AGU PUBLICATIONS

JGR

Journal of Geophysical Research: Oceans

RESEARCH ARTICLE

10.1002/2015JC011579

Key Points:
- SSH is estimated in the ice-covered and ice-free Arctic with bespoke radar altimeter data processing
- Arctic SSH is dominated by seasonal steric variation in response to summertime freshwater input
- Nonseasonal SSH variability dominated by bulging in the Beaufort Sea due to freshwater accumulation

Supporting Information:
- Supporting Information S1
- Supporting Information S2

Correspondence to:
T. W. K. Armitage,
tarmitage@ucl.ac.uk

Citation:
Armitage, T. W. K., S. Bacon, A. L. Ridout, S. F. Thomas, Y. Aksenov, and D. J. Wingham (2016), Arctic sea surface height variability and change from satellite radar altimetry and GRACE, 2003–2014, *J. Geophys. Res. Oceans*, *121*, 4303–4322, doi:10.1002/2015JC011579.

Received 17 DEC 2015
Accepted 24 MAY 2016
Accepted article online 27 MAY 2016
Published online 24 JUN 2016

Arctic sea surface height variability and change from satellite radar altimetry and GRACE, 2003–2014

Thomas W. K. Armitage[1], Sheldon Bacon[2], Andy L. Ridout[1], Sam F. Thomas[1], Yevgeny Aksenov[2], and Duncan J. Wingham[1]

[1]Centre for Polar Observation and Modelling, University College London, London, UK, [2]National Oceanography Centre, Southampton, UK

Abstract Arctic sea surface height (SSH) is poorly observed by radar altimeters due to the poor coverage of the polar oceans provided by conventional altimeter missions and because large areas are perpetually covered by sea ice, requiring specialized data processing. We utilize SSH estimates from both the ice-covered and ice-free ocean to present monthly estimates of Arctic Dynamic Ocean Topography (DOT) from radar altimetry south of 81.5°N and combine this with GRACE ocean mass to estimate steric height. Our SSH and steric height estimates show good agreement with tide gauge records and geopotential height derived from Ice-Tethered Profilers. The large seasonal cycle of Arctic SSH (amplitude ~5 cm) is dominated by seasonal steric height variation associated with seasonal freshwater fluxes, and peaks in October–November. Overall, the annual mean steric height increased by 2.2 ± 1.4 cm between 2003 and 2012 before falling to circa 2003 levels between 2012 and 2014 due to large reductions on the Siberian shelf seas. The total secular change in SSH between 2003 and 2014 is then dominated by a 2.1 ± 0.7 cm increase in ocean mass. We estimate that by 2010, the Beaufort Gyre had accumulated 4600 km^3 of freshwater relative to the 2003–2006 mean. Doming of Arctic DOT in the Beaufort Sea is revealed by Empirical Orthogonal Function analysis to be concurrent with regional reductions in the Siberian Arctic. We estimate that the Siberian shelf seas lost ~180 km^3 of freshwater between 2003 and 2014, associated with an increase in annual mean salinity of 0.15 psu yr^{-1}. Finally, ocean storage flux estimates from altimetry agree well with high-resolution model results, demonstrating the potential for altimetry to elucidate the Arctic hydrological cycle.

1. Introduction

The Arctic is experiencing some of the most rapid climatic changes on Earth [*IPCC*, 2013] including the reduction of sea ice extent [e.g., *Stroeve et al*., 2012] and the emergence of Arctic amplification [e.g., *Serreze et al*., 2009; *Serreze and Barry*, 2011]. Sea surface height (SSH) is an important global ocean climate indicator [*IPCC*, 2013], however, it is poorly observed in the Arctic. Tide gauge records are relatively sparse in space and time, and most are situated along the coasts of the Siberian and Scandinavian Arctic. *Proshutinsky et al*. [2004] have used tide gauges to estimate secular sea level change in the Siberian Arctic of 1.85 mm/yr between 1954 and 1989, and *Richter et al*. [2012] estimate trends of 1.3–2.3 mm/yr along the Norwegian coast between 1960 and 2010. Furthermore, conventional processing of satellite radar altimetry breaks down in the presence of sea ice, meaning that SSH in large areas of the Arctic and adjacent seas is not routinely monitored. This has meant that conventional altimeter studies of Arctic SSH have been limited to the open ocean [e.g., *Prandi et al*., 2012].

Bespoke satellite altimeter processing, originally developed by *Laxon* [1994], has allowed the extraction of SSH and sea ice thickness in the Arctic. *Laxon and McAdoo* [1994] used Arctic SSH to derive marine gravity anomalies and *Peacock and Laxon* [2004] used ERS altimeter data to construct a mean sea surface of the ice-covered Arctic Ocean. Annual changes in SSH from the ERS and Envisat radar altimeters were used by *Giles et al*. [2012] to estimate that the Beaufort Gyre accumulated 8000 ± 2000 km^3 of freshwater in the 2000s and *Bulczak et al*. [2015] used monthly data from Envisat to investigate seasonal SSH variability in the Nordic Seas. As well as altimetry, the twin Gravity Recovery and Climate Experiment (GRACE) satellites have provided global gridded monthly ocean mass—equivalent to ocean bottom pressure (OBP)—since 2002. These data have been used to study trends in the Arctic Ocean mass distribution [*Morison et al*., 2007], the seasonal cycle of Arctic Ocean mass [*Peralta-Ferriz and Morison*, 2010], nonseasonal variability of Arctic Ocean mass [*Volkov and Landerer*, 2013], and Arctic Ocean circulation [*Peralta-*

Ferriz et al., 2014]. *Morison et al*. [2012] combined Dynamic Ocean Topography (DOT) derived from ICESat laser altimetry with GRACE-derived OBP to investigate how changing circulation has affected freshwater distribution and storage in the Arctic. Despite coverage up to 81.5°N since 1991 and up to 88°N since 2010, Arctic SSH seasonal variability and the steric height contribution to Arctic SSH remain unresolved.

Enhancement of Arctic freshwater outflow may be able to disrupt the North Atlantic Meridional Overturning Circulation [*Manabe and Stouffer*, 1995], and has been linked to the North Atlantic "Great Salinity Anomalies" of the 1970s, 1980s, and 1990s [*Dickson et al*., 1988; *Belkin et al*., 1998; *Belkin*, 2004]. Given that the Arctic stores ~84,000 km^3 of freshwater in its surface layer [*Serreze et al*., 2006], and that the "Great Salinity Anomaly" of the 1970s consisted of only ~2000 km^3 excess liquid and solid freshwater export to the North Atlantic [*Häkkinen*, 1993], monitoring the balance of the Arctic Ocean freshwater fluxes is climatically important. Measurements from moorings, ships and Ice-Tethered Profilers (ITPs) have shown that the deep Arctic basins, in particular the Canada Basin, accumulated up to ~10,000 km^3 of freshwater during the 1990s and 2000s [*Proshutinsky et al*., 2009; *Krishfield et al*., 2014; *Rabe et al*., 2014]. *Tsubouchi et al*. [2012] used hydrographic data across the major openings to the Arctic Ocean to derive a picture of Arctic Ocean boundary fluxes for the first time. Since changes in SSH reflect fluctuations in ocean volume, basin-wide estimates of Arctic SSH can add an important element to our current understanding of the Arctic hydrological cycle.

There is evidence of a large seasonal cycle of Arctic SSH. Simply by considering the balance of annual freshwater sources and sinks, *Aagaard and Carmack* [1989] estimated an annual net "yield" of 9 cm for the central Arctic basin. By considering seasonal freshwater fluxes from precipitation and runoff, *Serreze et al*. [2006] showed that the Arctic Ocean seasonal cycle of liquid freshwater storage is at least as large as recent secular changes. *Bacon et al*. [2015] estimated an ocean storage flux cycle of roughly ±50 mSv to/from the central Arctic. Scaling by the size of the central Arctic basin (~10^{13} m^2), a volume flux of 50 mSv over 6 months of the year represents a change in mean SSH of ~8 cm. Results from tide gauges show that the Russian shelf seas have very large seasonal SSH variations [*Proshutinsky et al*., 2004]. A study of Arctic SSH using the ICESat laser altimeter only examined SSH in February and March [*Kwok and Morison*, 2011], leaving seasonal variability unresolved, and showed quite variable coverage, particularly close to the coast and on the Siberian shelf seas, due to a sparsity of lead returns. *Kwok and Morison* [2015] and *Mizobata et al*. [2016] used 4 and 5 years of CryoSat-2 data, respectively, to examine DOT of the ice-covered Arctic Ocean, leaving the full seasonal variability in seasonally ice-free regions unresolved. Ship-based hydrographic surveys of the shelf seas can only take place during the ice-free summer months [*Dmitrenko et al*., 2008] while observations from moorings and ITPs are limited to the deep basin [*Rabe et al*., 2014]. Satellite radar altimetry offers the chance to study the full seasonal cycle of SSH in the ice-covered and ice-free Arctic Ocean, particularly on the Siberian shelf seas, which annually receive ~2000 km^3 of freshwater via river runoff.

In this paper, we aim to reveal the seasonal and interannual SSH variability of the ice-covered and ice-free Arctic Ocean and to decompose the SSH budget to examine its steric and eustatic components. By doing so, we wish to investigate the relative importance of steric and eustatic effects at seasonal and interannual time scales; examine the effect of freshwater exchanges on Arctic Ocean SSH at seasonal and interannual time scales; elucidate the seasonal cycle of SSH in regions of seasonal or perennial ice cover where it has thus far been poorly resolved; and demonstrate satellite altimetry as a viable measurement tool to help monitor the hydrology of the Arctic Ocean. The paper is structured as follows: in section 2, we briefly outline the data, and in section 3, we describe the methodology used to derived monthly DOT over both the ice-covered and ice-free Arctic Ocean, how this is combined with GRACE ocean mass to estimate steric height and we estimate the monthly uncertainty. Section 4 presents the major results of this study: an evaluation of the data against tide gauge records and geopotential height calculated from ITPs, the Arctic Ocean mean DOT between 2003 and 2014, regional SSH, ocean mass and steric height time series and SSH spatiotemporal variability. In section 5, we discuss the Arctic SSH seasonal cycle and secular changes, regional freshwater exchanges and nonseasonal ocean mass variability on the Siberian shelf seas. Concluding remarks are provided in section 6.

2. Data

2.1. Radar Altimetry

We use data from the RA-2 radar altimeter carried by the Envisat satellite between March 2002 and April 2012, and the Synthetic Aperture Radar Interferometric Radar Altimeter (SIRAL) onboard the CryoSat-2

satellite, from April 2010 to date, which together span the entire GRACE OBP time series. RA-2 is a conventional pulse-limited Ku-band altimeter whereas over sea ice SIRAL applies along-track SAR processing to reduce the along-track footprint size to ~300 m [*Wingham et al.*, 2006]. Level-1b data are used in this study as the processing requires the full high rate record of altimeter waveforms.

2.2. GRACE

The GRACE mission comprises two satellites launched in 2002 that orbit in tandem, separated by 220 km. Small deviations in the separation are used to infer the Earth's gravity field, which can then be monitored over time to estimate changes in land water storage, ice sheet mass, ocean mass, and glacial isostatic adjustment. We use Release-05 gridded GRACE ocean mass products from the Jet Propulsion Laboratory [*Chambers and Bonin*, 2012] that have been smoothed with a 500 km radius Gaussian filter and are provided in units of centimeters of water height equivalent.

2.3. In Situ Data

Tide gauge records of SSH taken from the Permanent Service for Mean Sea Level [*Holgate et al.*, 2013] are used to evaluate altimeter-derived SSH estimates. Monthly mean sea level is provided for each tide gauge location relative to a local reference frame. Hydrographic profiles (pressure, temperature, and salinity) collected by ITPs are used to derive geopotential height, which is compared against steric height estimates from altimetry and GRACE. ITPs consist of a buoy tethered to an ice floe, with a wire extending through the ice and into the ocean where it is weighted down to a depth of ~500–800 m. A profiler then cycles up and down the wire collecting temperature and salinity measurements [*Toole et al.*, 2011].

3. Methods

3.1. Deriving SSH

The altimeter SSH processing is based on the work of Peacock and Laxon [2004] and *Giles et al.* [2012]; the methods developed in those papers are here applied to RA-2 and SIRAL. SSH is measured by altimeters as the height of the ocean surface above the reference ellipsoid:

$$\mathrm{SSH} = A - (R + H_{retrack} + \Sigma H_{corr}) \tag{1}$$

where A is the satellite altitude relative to the WGS84 ellipsoid, R is the satellite range to the surface (estimated from the two-way range window delay) and $H_{retrack}$ is the retracker correction to account for the range difference between the waveform leading edge and the range window tracking point. ΣH_{corr} is the sum of the tidal and atmospheric geophysical corrections (dry and wet troposphere, ionosphere, inverse barometer/dynamic atmosphere correction, ocean tide, long period tide, solid Earth tide, and geocentric polar tide) that must be removed from SSH estimates before they are analyzed. We take the geophysical corrections from the European Space Agency data products and apply them in the conventional way according the Level-1b to Level-2 processing specifications provided in the Envisat and CryoSat-2 user documentation [*Soussi et al.*, 2011; *European Space Agency*, 2015]. The sea level anomaly (SLA) is then SSH referenced to a long-term mean sea surface (MSS):

$$\mathrm{SLA} = \mathrm{SSH} - H_{MSS} \tag{2}$$

where H_{MSS} is the height of the MSS interpolated to individual measurement locations. Here we make use of the high-resolution MSS used by *Laxon et al.* [2013] to calculate sea ice freeboard, which has been updated to include 2 years of along-track lead and open ocean CryoSat-2 SSH estimates acquired between September 2011 and September 2013 [*Ridout*, 2014]. The offset in elevation between lead and open ocean estimates is removed by inspecting the elevation change at the ice edge (see below). This MSS has a horizontal spatial resolution of 5 km and captures very short wavelength ocean height undulations caused by marine gravity anomalies that reflect the tectonic history of the seafloor [*Laxon and McAdoo*, 1994]. Referencing SSH to this MSS "flattens" SSH profiles as much as possible, originally for the purpose of estimating sea ice freeboard [*Laxon et al.*, 2013]. DOT is SSH relative to the geoid:

$$\mathrm{DOT} = \mathrm{SSH} - H_{geoid} \tag{3}$$

where H_{geoid} is the geoid height interpolated to individual measurement locations. We use the GOCO03s combined satellite-only geoid derived from GOCE and GRACE data, CHAMP and GOCE kinematic orbits, and

satellite laser ranging [*Mayer-Gürr et al*., 2012]. GOCO03s does not contain any altimeter data (unlike, e.g., the EGM2008 geoid) which could contaminate the geoid model with a residual ocean signal [*Farrell et al*., 2012].

In sea ice covered regions, specular echoes originating from leads are identified using waveform pulse peakiness, leading edge width and, for CryoSat-2, the beam stack standard deviation [*Peacock and Laxon*, 2004; *Laxon et al*., 2013]. Lead echoes are retracked using the "Gaussian + exponential" model originally developed by *Giles et al*. [2007], that has successfully been applied to Envisat [*Giles et al*., 2008] and CryoSat-2 [*Laxon et al*., 2013] lead echoes in order to derive SSH for estimating sea ice freeboard. This retracker can be applied to both altimeters despite their different operating modes. Leads dominate echoes even if they only cover a small fraction of the footprint, reducing the effective illumination area of the altimeter footprint [*Drinkwater*, 1991]. This has the effect of reducing the instrument impulse response to a delta function, which, when combined with very small surface roughness, means that the echo received from leads is essentially a copy of the transmit pulse [*Kurtz et al*., 2014]. Over the open ocean, we use the ocean retracking correction supplied in the distributed data products for Envisat and CryoSat-2 Low-Resolution Mode (LRM). For CryoSat-2 SAR mode data over the open ocean, we use a 70% first threshold retracking point.

We calculate the bias associated with using different retracking methods over different surface types (the lead/open ocean bias introduced by *Giles et al*. [2012]). Separate biases are calculated for Envisat and CryoSat-2 due to the different operating modes. Estimates of SLA (equation (2)) from leads and from the open ocean are spatially averaged on separate $2^\circ \times 0.5^\circ$ longitude-latitude grids for each month. Using SLA here (rather than SSH or DOT) minimizes the potential error due to ocean surface slope over horizontal scales smaller than the grid size. The lead and open ocean SLA grids are differenced for each month to obtain monthly grids of the offset between lead-derived SLA and open ocean SLA and grid cells are masked if they are within 10 km of land to avoid issues with land contamination. The monthly mean lead/open ocean bias is calculated from each monthly grid of offsets and the long-term mean lead/open ocean bias is then added to all lead-derived SSH estimates, after *Giles et al*. [2012]. We find that the residual monthly lead/open ocean bias varies seasonally and is larger by ~1–4 cm between June and November for both missions. We hypothesize that this is caused by the presence of melt ponds and the exposure of bare ice between June and August and the formation of thin new ice between September and November. All of these surfaces can give rise to specular "lead-type" waveforms, biasing the lead-derived SSH high. Thus, we also estimate a mean seasonally varying lead/open ocean bias (i.e., 12 values, one for each month) and remove this from all lead SSH estimates.

Data from the two missions are cross calibrated in the mission overlap period: the first full month of CryoSat-2 data came in November 2010 and the last full month of Envisat data was March 2012. Monthly SLA estimates, incorporating both lead-derived and open ocean SSH, for each mission are spatially averaged on a $2^\circ \times 0.5^\circ$ grid and the 10 km land mask applied. The monthly mean difference in SLA measured by Envisat and CryoSat-2 is estimated by averaging all grid cells between 60°N and 81.5°N. It was found that CryoSat-2 SLA estimates were 4.2 cm lower than Envisat on average and this time mean inter-satellite offset was removed from the CryoSat-2 data, taking the Envisat time series as the benchmark because it is well calibrated against Jason-1/2 for studies of sea level change [*Ollivier et al*., 2012]. There is some residual spatial variability of the inter-satellite offset due mainly to the different orbits of the two satellites, which means that they sample the ocean surface height (and the associated

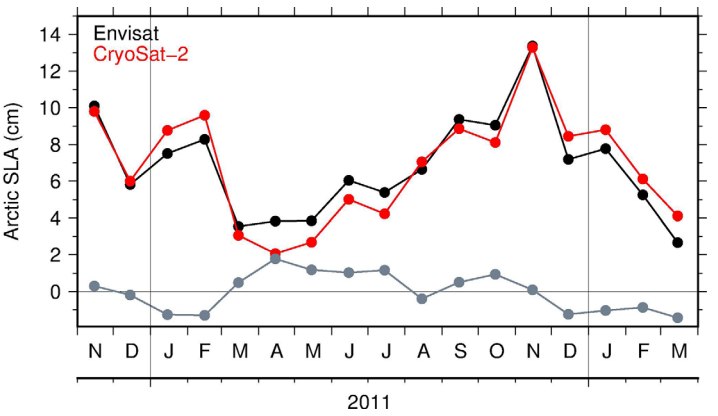

Figure 1. Arctic mean SLA from Envisat (black) and CryoSat-2 (red) between 60°N and 81.5°N between November 2010 and April 2012 and the difference (gray) after removal of the time mean inter-satellite offset of 4.2 cm.

time-varying DOT and geophysical corrections) at different times throughout a given month (supporting information Figure S1). The residual spatial variability is of order 1–2 cm in the deep ocean, with larger magnitudes over shelf sea areas where tide solutions are poorer. The mean SLA in the mission overlap period is shown in Figure 1 after removal of the time mean inter-satellite offset of 4.2 cm. The agreement between Envisat and CryoSat-2 is very good, with R = 0.94 and a root-mean-square (RMS) difference of 1.0 cm.

3.2. Estimating Steric Height

Changes in ocean volume, and hence SSH, comprise a sum of two components: eustatic, due to changes in ocean mass, and steric, due to changes in ocean density. Eustatic changes arise, for example, through exchange of water with land, atmospheric precipitation and evaporation, unbalanced ocean fluxes entering or leaving a region, or locally, via changes in surface forcing causing accumulation or release of water from a region. Changes in ocean density result from changes in ocean temperature and salinity. At low water temperatures, as in the Arctic, changes in steric height are dominated by changes in salinity. It is possible to estimate steric height by combining data from altimeters, which measure the total SSH, and GRACE, which is only sensitive to changes in ocean mass. Monthly DOT estimates (equation (3)) are spatially averaged on the $2^\circ \times 0.5^\circ$ grid and the 10 km land mask is applied. The gridded data are then smoothed with a Gaussian convolution filter with a standard deviation of 100 km and a radius of 3 standard deviations. Monthly GRACE ocean mass estimates must be corrected for the effect of globally averaged atmospheric pressure [see, e.g., *Peralta-Ferriz et al*., 2014]. We estimate monthly mean atmosphere sea level pressure anomalies over the global ocean from the ERA-Interim reanalysis [*Dee et al*., 2011]. The atmospheric pressure anomalies are converted to sea level equivalent by dividing by $\rho_0 g$, where $\rho_0 = 1,028$ kg m^{-3} and g is the gravitational acceleration, and are subtracted from the monthly GRACE ocean mass grids. This is largely a seasonal effect, with an amplitude of $\sim$0.8 cm, that must be accounted for in our analysis of seasonal ocean mass and steric height variability. The monthly GRACE ocean mass estimates are then gridded on the same $2^\circ \times 0.5^\circ$ grid as the monthly DOT data and the monthly gridded steric height is estimated by simply subtracting the gridded ocean mass from the gridded DOT.

When we estimate monthly regionally averaged ocean mass and steric height (section 4.3), gaps in the GRACE record must be accounted for as the satellites are periodically switched off for battery management. Over the 12 year time series, 13 months are missing, mostly after 2011. The mean ocean mass in missing months is interpolated using a weighted mean of 2 months either side of the missing month. The weighting assigns twice as much weight to the adjacent month as to the adjacent-but-one months i.e., [1, 2, NaN, 2, 1]. The missing monthly mean steric height is then simply the monthly mean DOT minus the interpolated monthly mean ocean mass.

3.3. The "Pole Hole"

We define the central Arctic Ocean as the region bounded by Fram Strait, the Barents Sea Opening, Bering Strait, Nares Strait, and the north of the Canadian Arctic Archipelago (CAA, Figure 2). Baffin Bay is excluded from the present analysis to eliminate the local residual contamination of GRACE data by the large terrestrial mass loss signals of the Greenland Ice Sheet and CAA ice caps [*Chambers and Bonin*, 2012]. In practice, 27% of this defined area is not sampled by Envisat (Figure 2) so to ensure compatibility over the whole time series, the GRACE and CryoSat-2 data are truncated at 81.5°N. However, there are now over 4 years of CryoSat-2 altimetry data up to 88°N with which to assess whether the monthly mean DOT calculated up to 81.5°N is representative of the whole basin. First, the mean DOT within our defined boundary was calculated between November 2010 and December 2014 both north and south of 81.5°N to determine whether variations north of 81.5°N are coherent with variations in the rest of the study area. The seasonal cycle has a similar magnitude and phase north and south of 81.5°N and there is a static offset of $\sim$10 cm. The static offset simply reflects the fact the Beaufort Gyre lies in the region south of 81.5°N. When variability with periods of 12 months and longer is filtered out, we find R = 0.65 between the monthly SSH variations (supporting information Figure S2).

The monthly mean DOT was then calculated using all CryoSat-2 data south of 88°N, and just data south of 81.5°N to determine the impact of the inclusion of data north of 81.5°N on the basin mean DOT (supporting information Figure S3). The mean difference of 2.39 cm simply reflects the fact that not including data in the "pole hole" puts more weight on the higher DOT in the Beaufort Gyre. A correlation of R = 0.98 and an RMS difference of 0.69 cm, together with good correlation between month-to-month variations north and

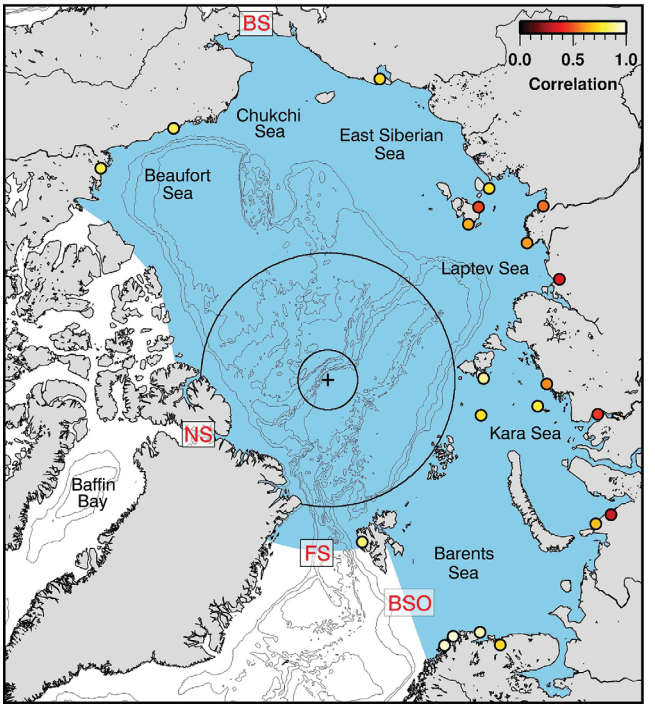

Figure 2. Map of the Arctic Ocean. The blue shaded region represents our study area and is enclosed by the north of the Canadian Arctic Archipelago, Fram Strait (FS), Barents Sea Opening (BSO), Bering Strait (BS), and Nares Strait (NS). The lines at 81.5°N and 88°N represent the latitudinal limits of the Envisat and CryoSat-2 satellites, and isobaths taken from the ETOPO1 global bathymetry model are drawn at 1000 m intervals [*Amante and Eakins*, 2009]. Tide gauge locations are shown by circles colored by the correlation with altimeter SSH (Table 1).

south of 81.5°N, gives us confidence that temporal variations in mean SSH south of 81.5°N are representative of variations across the whole basin at monthly to seasonal time scales (see section 5.2 for discussion on secular changes). We add (root-sum-square) the RMS difference of 0.69 cm to our estimates of the monthly and annual mean SSH uncertainty to account for the uncertainty associated with only sampling south of 81.5°N. We hypothesize that our results are so insensitive (at least at monthly/seasonal time scales) to excluding the high Arctic because this is a region of low surface forcing and low surface forcing variability. Modeled estimates of Arctic Ocean surface stress have been found to be relatively small north of 81.5° with little variation over the course of a year [*Martin et al.*, 2014]. Over interannual time scales, however, the high Arctic is responsive to surface forcing [*Morison et al.*, 2006] and we discuss longer-term changes of SSH north of 81.5°N in section 5.2.

We have repeated the above analysis with the GRACE data and find similarly good agreement between the data north and south of 81.5°N. There is good coherence between both the seasonal and deseasonalized time series north and south of 81.5°N (supporting information Figure S4) and there is an RMS difference of 0.52 cm between basin mean ocean mass estimates that include or exclude data north of 81.5°N (supporting information Figure S5). We add the RMS difference to our monthly and annual estimates of the GRACE uncertainty.

3.4. Uncertainty Estimates

The monthly and annual mean SSH uncertainties are calculated from the RMS difference in SSH at orbit crossover locations [*Peacock and Laxon*, 2004], using the method of *Giles et al.* [2012]. The difference in SSH at crossover locations is made up of several components: the instantaneous DOT, errors in the tidal and atmospheric geophysical corrections, instrumental noise, and orbit error. By calculating the SSH uncertainty in this way, we intend to account for all the components of SSH uncertainty without prescribing values to the individual components, which are difficult to determine in the Arctic Ocean where there is a lack of independent data with which to assess each term. The RMS difference in SSH at orbit crossover locations separated in time by 15 days or more is estimated for each month of data. While each of the individual error contributions will decorrelate over different time and spatial scales, we expect them all to be decorrelated over a period of 15 days. The mean RMS crossover difference over our Arctic Ocean domain (Figure 2) is calculated and the monthly mean uncertainty is estimated by dividing by the square root of the number of valid Arctic passes (typically around 400 per month). The resulting mean monthly uncertainty is 0.6 cm for both satellites (supporting information Figure S6). There is no significant difference between the Envisat and CryoSat-2 RMS crossover difference because the errors are dominated by noninstrumental errors including errors in the geophysical corrections (especially tide model error) and orbit errors (since orbits are less well determined at the poles). To this we add (in quadrature): (1) the standard error of the lead/open ocean bias; (2) the standard error of the inter-satellite bias; (3) the uncertainty associated with only sampling south of 81.5°N. The mean monthly and annual SSH uncertainty is then 1.1 and 0.9 cm, respectively.

Table 1. Comparison of Monthly Altimeter and Tide Gauge SSH Estimates[a]

Station	Location	D (km)	N	Slope	Std (cm)	R
Vardø	(31.1°E, 70.4°N)	76	132	0.79	4.1	0.92
Honningsvåg	(26.0°E, 71.0°N)	57	132	0.82	3.0	0.96
Hammerfest	(23.7°E, 70.7°N)	93	131	0.80	3.3	0.95
Murmansk	(33.0°E, 69.0°N)	162	127	0.61	7.3	0.73
Barents Sea		**97**	**131**	**0.76**	**4.4**	**0.89**
Amderma	(61.7°E, 69.8°N)	84	131	0.52	8.3	0.68
Ust	(64.5°E, 69.2°N)	85	117	0.25	12.0	0.31
Vise	(77.0°E, 79.5°N)	58	97	0.57	5.6	0.75
Sopochnaia	(82.7°E, 71.9°N)	239	103	0.27	11.7	0.44
Izvestia	(82.9°E, 75.9°N)	57	128	0.79	8.0	0.80
Sterlegova	(88.9°E, 75.4°N)	69	93	0.42	10.9	0.58
Golomianyi	(90.6°E, 79.6°N)	53	89	0.94	4.6	0.89
Kara Sea		**92**	**108**	**0.54**	**8.7**	**0.64**
Anabar	(113.5°E, 73.2°N)	117	132	0.17	11.0	0.36
Dunai	(124.5°E, 73.9°N)	46	101	0.47	10.4	0.61
Tiksi	(128.9°E, 71.6°N)	146	84	0.38	11.8	0.54
Kotelnyi	(137.9°E, 76.0°N)	55	129	0.67	10.8	0.64
Sannikova	(138.9°E, 74.7°N)	78	108	0.44	12.1	0.47
Kigiliah	(139.9°E, 73.3°N)	62	113	0.70	9.0	0.74
Pevek	(170.2°E, 69.7°N)	89	97	0.61	10.0	0.73
Laptev and E. Siberian Seas		**85**	**109**	**0.49**	**10.7**	**0.58**
Tuktoyaktuk	(133.0°W, 69.4°N)	126	99	0.65	6.4	0.81
Prudhoe	(148.5°W, 70.4°N)	69	139	0.58	5.3	0.82
Beaufort Sea		**98**	**119**	**0.62**	**5.9**	**0.82**
Ny-Ålesund	(11.9°E, 78.9°N)	84	132	0.70	3.9	0.86

[a]For each station, we show the distance between the altimeter grid cell and tide gauge location, D, the number of months available for comparison, N, the slope of a linear fit between the altimeter and tide gauge scatterplot (supporting information 2), the standard deviation of the residual between the altimeter SLA and the linear fit to the tide gauge sea level, and the correlation coefficient, R. Shown in bold is the mean for the Barents, Kara, Laptev and East Siberian, and Beaufort Seas (Ny-Ålesund is on Svalbard).

The monthly mean GRACE ocean mass uncertainty north of 65°N is 0.9 cm according to *Volkov and Landerer* [2013]; however, we use the more conservative estimate of 1.5 cm after *Chambers and Bonin* [2012]. Accounting for the additional uncertainty due to not including data north of 81.5°N, the monthly ocean mass uncertainty is 1.6 cm. The annual mean ocean mass uncertainty is then 0.5 cm. Combining the altimeter and GRACE uncertainty gives monthly and annual steric height uncertainties of 1.9 and 1.0 cm, respectively.

4. Results

4.1. Evaluating Altimeter SSH

GRACE Arctic Ocean mass variations have been independently evaluated against Bottom Pressure Recorders as well as tide gauges and modeled ocean mass variations [*Peralta-Ferriz and Morison*, 2010; *Peralta-Ferriz et al*., 2014]. Here we evaluate monthly altimeter SSH estimates against tide gauges and steric height against geopotential height (GPH) derived from ITPs.

4.1.1. Tide Gauges

We use data from tide gauge stations within our defined Arctic Ocean basin (Figure 2) that have $\geq$ 72 months of data available in the period 2003–2014, i.e., half or more of the full time series. The tide gauge data supplied by the Permanent Service for Mean Sea Level have only had the effects of diurnal and semidiurnal tides filtered out and are provided as monthly mean sea level heights. Thus, to make a more like-for-like comparison, it is necessary to omit the inverse barometer/dynamic atmosphere and long period tidal corrections from equation (1) because these corrections have not been applied to the tide gauge data. Monthly SLA estimates are spatially averaged on the 2° $\times$ 0.5° grid, the 10 km land mask is applied, and a Gaussian convolution filter with standard deviation of 50 km and width of 300 km is applied. Since tide gauges are essentially point measurements, very close to the coast, it is desirable to filter the SLA as little as possible for the purpose of this comparison. We then simply compare the tide gauge SSH against the closest filled altimeter grid cell. Individual tide gauge comparison plots are provided in supporting information 2 and are summarized numerically in Table 1.

The mean difference between the tide gauge and altimeter SLA is removed. We calculate the slope of a linear fit to the scatter between the tide gauge and the altimetry data and the standard deviation of the residual between the altimeter SLA and the linear fit (supporting information 2). The correlation between the altimeter and tide gauge data is significantly nonzero (p value $\ll 1$) for all of the available tide gauge records, and is shown in Figure 2. There is excellent correlation (R = 0.89) in the Barents Sea region. The poorer agreement at the Murmansk station in the Barents Sea (R = 0.73) is likely due to the larger separation between the tide gauge and the nearest available altimeter data. In fact, the time series with some of the lowest correlations (Ust, Sopochnaia, Anabar, Dunai, and Tiksi) are estuarine and prone to large sea level variations due to seasonal runoff [*Proshutinsky et al*., 2004] which would not necessarily be detected by the altimeter data due to the application of the land mask. An example of this can be seen in the time series at the Anabar station which show good agreement between 2003–2006 and 2012–2013, but the altimetry data do not capture large summer spikes present in the tide gauge SSH between 2007 and 2011 (supporting information 2). In the Kara, Laptev, and East Siberian Seas, where the effects of seasonal runoff are greatest, the mean scatterplot slope is smaller (0.49 compared to 0.62 for the rest of the basin) and the mean residual standard deviation is higher (10.7 cm compared to 6.7 cm for the rest of the basin), but despite this, there is still good overall correlation (R = 0.58). There is very good agreement between the altimeter SSH and the tide gauges in the Beaufort Sea (R = 0.82) and the Ny-Ålesund tide gauge on Svalbard (R = 0.86). Overall, in regions of seasonal sea ice cover, there is good correlation (R = 0.65) between the altimeter SSH and tide gauge SSH lending confidence to the method of (1) combining lead and open ocean SSH measurements over the course of the year and (2) extending the altimeter time series using multiple satellite missions.

4.1.2. Hydrographic GPH

Hydrographic profiles (pressure, temperature, and salinity) collected by ITPs can be used to validate the steric height derived from altimeter and GRACE data. This is similar to the comparisons between satellite-derived DOT and hydrographic GPH presented by *Kwok and Morison* [2011], *Kwok and Morison* [2015], and *Mizobata et al*. [2016] with the difference that here we compare directly with steric height rather than DOT. First, the specific volume anomaly, δ, is calculated over an ITP profile as:

$$\delta = v_s(S,T,p) - v_s(35,0,p) \tag{4}$$

where $v_s(S,T,p) = \rho(S,T,p)^{-1}$ is the specific volume for density ρ, at salinity, S, temperature, T, and pressure, p [*Gill*, 1982]. This is then integrated from the surface down to pressure, p_0, to give the geopotential height:

$$\mathrm{GPH} = \int_0^{p_0} \delta dp \tag{5}$$

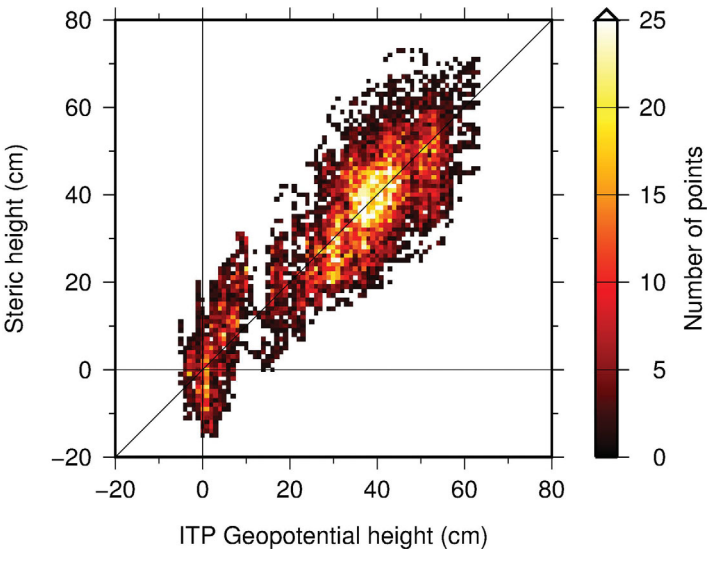

Figure 3. Scatterplot of the satellite-derived steric height against the GPH derived from ITP data. Note that, since GPH is not an absolute measurement, the difference between the mean steric height and the mean GPH is removed from the GPH estimates.

We integrate down to $p_0 = 500$ dbar (roughly 500 m) and we only perform the integration when the shallowest pressure recording is less than 10 dbar and the deepest pressure recording is greater than 500 dbar. Estimates of GPH from each month between 2004 and 2014 are spatially averaged on the same 2° × 0.5° grid as the monthly grids described in section 3.2 and the satellite-derived steric height is interpolated to the mean location of the ITP profiles in each grid cell. There is good agreement between the satellite-derived steric height and the ITP-derived GPH with R = 0.87 and an RMS difference

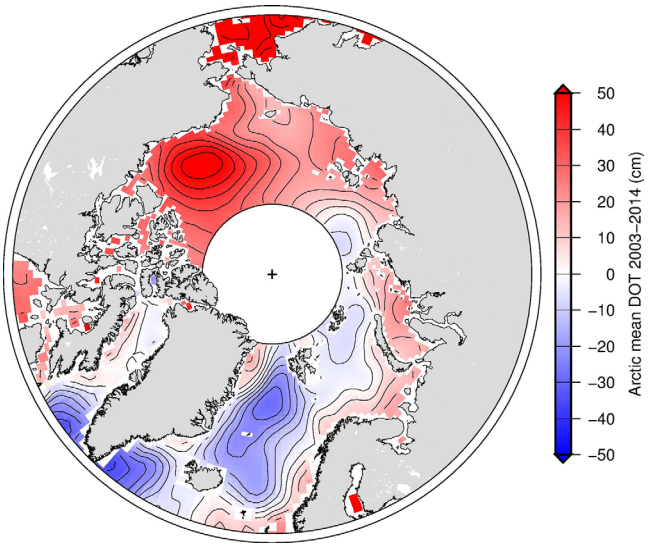

Figure 4. The 2003–2014 Arctic mean DOT. Contours are drawn every 5cm and the solid circle at 81.5°N represents the latitudinal limit of the Envisat satellite.

of 8.4 cm over a range of ~80 cm (Figure 3). The steric height (i.e., altimetry minus GRACE) shows a better agreement than the altimetry data on its own. The spread in Figure 3 is likely caused by the relatively low resolution of the GRACE data and the smoothing applied to the altimetry whereas the ITP data will be sensitive to small-scale transient ocean features.

4.2. Arctic Ocean Mean Dynamic Topography

The time mean DOT (MDT) reflects the long-term dynamically driven departure of SSH from the geoid, and hence the time mean ocean geostrophic circulation. The monthly grids of DOT described in section 3.2 were averaged over time to estimate the 2003–2014 Arctic MDT (Figure 4). The GOCO03s geoid is calculated up to spherical harmonic degree/order 250 meaning that it should be able to resolve features with wavelength of order 80 km. By inspecting transects of the MDT, it was determined that the Gaussian convolution filter used to smooth the monthly DOT grids successfully removes undulations due to short wavelength noise in the geoid model. The main features of the Arctic MDT are clearly visible: a high in the Beaufort Sea associated with the anticyclonic Beaufort Gyre, a low in the Greenland Sea associated with the cyclonic Greenland Sea gyre and a large-scale slope of DOT from the Amerasian Basin to the Eurasian Basin associated with the transpolar current. This result agrees qualitatively well with previous results from satellite altimetry [*Kwok and Morison*, 2011; *Farrell et al*., 2012; *Giles et al*., 2012; *Kwok and Morison*, 2015] and models [e.g., *Koldunov et al*., 2014; *Proshutinsky et al*., 2015].

4.3. Regional SSH, Ocean Mass, and Steric Height Variability

4.3.1. Arctic Overview

The mean Arctic SSH, ocean mass, and steric height are calculated monthly between January 2003 and December 2014 from the gridded fields described in section 3.2; Envisat data are used for 2003–2011 and CryoSat-2 for 2012–2014 (Figure 5). It was found that smoothing the altimetry data with the same smoothing function as the GRACE data did not significantly affect estimates of the mean SSH or steric height. Almost two thirds of the Arctic SSH variance found in our defined region occurs on length scales greater than the width of the smoothing applied to the GRACE data (the SSH variance structure is described in more detail in section 4.4 below). Thus, increasing the smoothing used on the altimeter data obscures short wavelength spatial variability but has a minimal effect on the basin mean SSH. We take the mean of the monthly DOT grids within our defined basin (Figure 2) and the time mean is removed from the resulting altimeter time series of Figure 5. Since the temporal variability of DOT is unaffected by the choice of reference surface, below we refer simply to SSH variability.

Seasonal variation in Arctic Ocean SSH must be distinguished from longer-term secular changes. To separate seasonal and secular variations, the monthly estimates of mean SSH, ocean mass, and steric height are filtered with a 12 month moving average and we then subtract the filtered from the unfiltered time series to obtain three residual time series. The mean seasonal cycles are calculated as the mean and standard deviation for each calendar month for the residual time series (Figure 5, right). Arctic Ocean SSH variability is dominated by the seasonal cycle, which is larger than the observed secular changes. The form of the SSH seasonal cycle from altimetry is similar to that observed by tide gauges [*Proshutinsky et al*., 2004; *Richter et al*., 2012], although the amplitude is smaller because (1) tide gauge SSH estimates include the inverse barometer and long-period tidal effects, which are removed from the altimetry data and (2) tide gauges measure SSH variations near the coast, where the seasonal cycle is largest (supporting information Figure

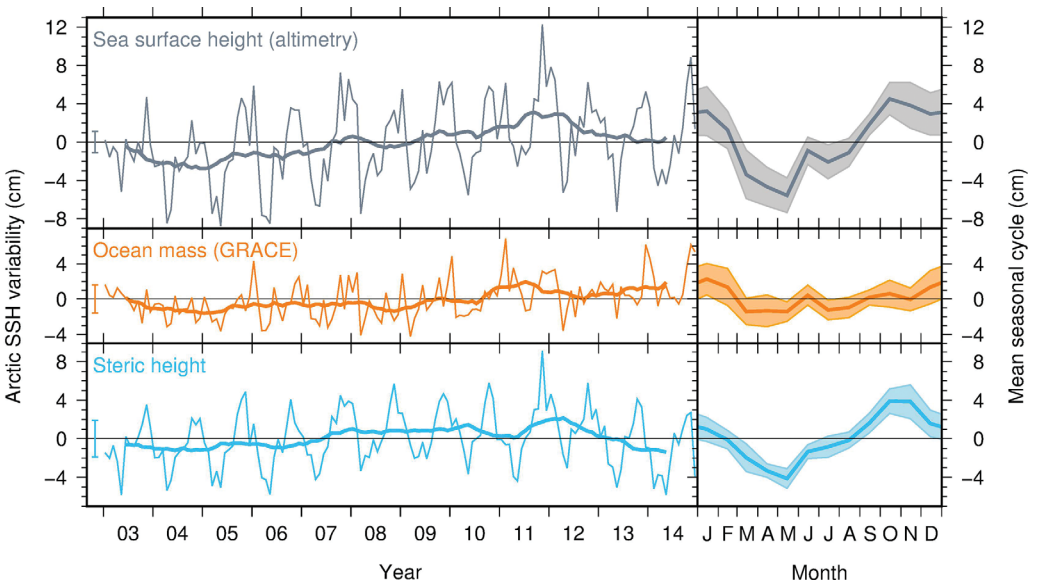

Figure 5. The monthly (left) mean time series and (right) the mean seasonal cycle (shaded region is ±1 standard deviation) of the SSH (grey), ocean mass (orange), and steric height (blue) in the Arctic Ocean between 2003 and 2014. The time mean has been removed from the altimetry and GRACE data. The 12 month running average is shown superimposed on top of monthly means (left, thick lines) and the monthly uncertainty estimate for each time series is shown adjacent to the left *y* axis.

S7), in particular on the Siberian shelf seas where many of the available tide gauge records are located (Figure 2 and supporting information 2).

The mean Arctic SSH seasonal cycle shows a broad maximum of +4cm between October–January, a minimum of −6 cm in May, and a relatively small, intermediate peak in June (Figure 5). The latter is also present in the seasonal cycle of ocean mass and has been linked to the annual cycle of river runoff [*Peralta-Ferriz and Morison*, 2010]. In their analysis of the Arctic Ocean mass seasonal cycle, *Peralta-Ferriz and Morison* [2010] found a summertime peak that is greater than the wintertime peak, unlike the results presented in Figure 5 where the wintertime peak dominates. There are three reasons for this apparent discrepancy. First, for both SSH and ocean mass, excluding data north of 81.5°N leads to an overestimate of the wintertime peak in the seasonal cycle relative to the summertime peak by ∼1 cm. Second, accounting for the globally averaged atmospheric pressure, which is largely a seasonal signal, increases the wintertime peak relative to the summertime peak. Finally, *Peralta-Ferriz and Morison* [2010] used GRACE data from August 2002 to May 2008, whereas we use data between January 2003 and December 2014. Including data from the "pole hole," not accounting for globally averaged atmospheric pressure as described in section 3.2, and using the same subset of data results in a June peak in ocean mass, as reported by *Peralta-Ferriz and Morison* [2010].

There was a spike in the SSH and steric height in November 2011 of ∼4 cm greater than the seasonal cycle. The November 2011 GRACE ocean mass was estimated using data only until 16 November, leading to an underestimate of the monthly mean value; see *Volkov and Landerer* [2013], who found a spike in ocean mass in modeled results that otherwise agreed very well with GRACE, and concluded that in fact there was a spike in ocean mass in November 2011. Such spikes are associated with simultaneous northward wind anomalies through the Fram and Bering Straits, which inhibit inflow through one Arctic Ocean gateway from being balanced by outflow through another [*Volkov and Landerer*, 2013; *Peralta-Ferriz et al*., 2014].

4.3.2. The Beaufort Gyre

Giles et al. [2012] focused on annual SSH changes in the Beaufort Gyre region, accounting for the ocean mass component to estimate the SSH contribution due to freshwater change. Here we present a monthly record of steric height in the Beaufort Gyre and estimate freshwater content (FWC) in the region 130°W–180°W and 70°N–81.5°N using the method of *Giles et al*. [2012], which assumes a fresh surface layer that sits on top of a denser, more saline layer at depth (Figure 6). FWC estimates are presented as an anomaly relative to the 2003–2006 mean as this allows us to compare our results to the Beaufort Gyre liquid FWC estimates of *Krishfield et al*. [2014]. The mean seasonal cycle and its interannual variability are estimated in the same way as in section 4.3.1.

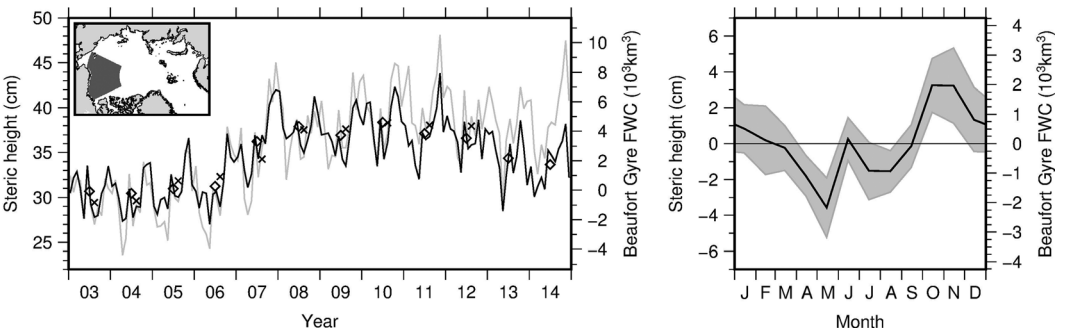

Figure 6. (left) The monthly mean steric height (black) in the Beaufort Gyre region (130°W–180°W, 70°N–81.5°N) for grid cells greater than 300 m depth. The equivalent freshwater content is shown on the right-hand axis relative to the 2003–2006 mean. Annual means are shown with diamonds and the August mean hydrographic liquid FWC anomalies (taken from *Krishfield et al*. [2014]; Table 2) are shown in crosses. Altimeter SSH (i.e., unadjusted for mass variations) is shown in gray. (right) The mean seasonal steric height/FWC cycle (shaded region is ±1 standard deviation).

The steric height in the Beaufort Gyre region increased between 2006 and 2008, with the largest increase occurring in late 2007 (Figure 6). Between 2008 and 2010, the steric height was 6.9 cm greater than the 2003–2006 mean, peaking in 2010 at 7.5 cm greater than the 2003–2006 mean. This corresponds to an increase in FWC of 4200 km^3 between 2008–2010 and 2003–2006, and a 2010 peak in FWC of 4600 km^3 greater than the 2003–2006 mean. These estimates show excellent agreement with liquid FWC change calculated from hydrographic observations: *Krishfield et al*. [2014] reported that between 2008 and 2010, liquid FWC was 4300 km^3 greater than the 2003–2006 mean and peaked in 2010 at 4600 km^3 greater than the 2003–2006 mean (Figure 6 and Table 2). Our estimates show a smaller total increase than estimated by *Giles et al*. [2012] as our time series is shorter, but our estimates of FWC change agree well after 2003. Extension of the time series up to 2014 shows that, while the annual mean SSH has remained roughly constant since 2008, and indeed peaked in late 2014, as the ocean mass component has increased, so the steric height component has decreased since 2011–2012. By 2014, the FWC was just 1700 km^3 greater than the 2003–2006 mean. *Proshutinsky et al*. [2015] showed, using the Arctic Ocean Oscillation index, that the Arctic has been in the Anticyclonic Circulation Regime since the late 1990s, which promotes Beaufort Gyre freshwater storage by Ekman convergence. Since 2011, the Anticyclonic Circulation Regime weakened relative to the high values seen through the middle of the decade 2000–2009 which we see reflected here as a decrease in steric height and release of ~2100 m^3 of freshwater from the Beaufort Gyre between 2011 and 2014.

The Beaufort Gyre region has a steric height seasonal cycle of ±3.5 cm that peaks in November with a secondary peak in June (Figure 6, right). By the method of *Giles et al*. [2012], this represents a FWC seasonal cycle of ±2000 km^3, equivalent to a freshwater layer depth of ±1.1 m. Using around 3 years of observations from four permanent moorings in the Beaufort Sea, *Proshutinsky et al*. [2009] found seasonal variability of ±1 m, with a similar, double-peaked cycle. Considering the difference in spatial and temporal coverage of the two data sets this represents a good agreement. On top of the annual sources and sinks of liquid FWC, the seasonal cycle of FWC in the Beaufort Gyre region is modulated by the seasonal cycle of wind stress curl which is a minimum in Autumn (maximum Ekman convergence) [*Proshutinsky et al*., 2009].

Table 2. Annual Mean FWC Estimates From This Study Compared to the August Hydrographic Liquid FWC Inventory of *Krishfield et al*. [2014, Table 3] Relative to the 2003–2006 Mean[a]

Year	This Study	*Krishfield et al*. [2014]
2003	−100	−800
2004	−200	−700
2005	100	600
2006	200	900
2007	3300	2100
2008	4300	4100
2009	3700	4200
2010	4600	4600
2011	3800	4400
2012	3500	4400
2013	2200	N/A
2014	1700	N/A

[a]The correlation between 2003 and 2012 is 0.95.

4.3.3. The Siberian Shelf Seas

The Siberian shelf seas receive ~2000 km^3 of river runoff between May and October [*Aagaard and Carmack*, 1989; *Serreze et al*., 2006] and thus play a central role in the Arctic freshwater cycle. However, ship-based observations of FWC on the Siberian shelf seas are generally limited to the "hydrographic summer" season [*Dmitrenko et al*., 2008] and FWC estimates from ITPs and other drifting stations are confined to the deep Arctic basins [*Rabe et al*., 2014]. As

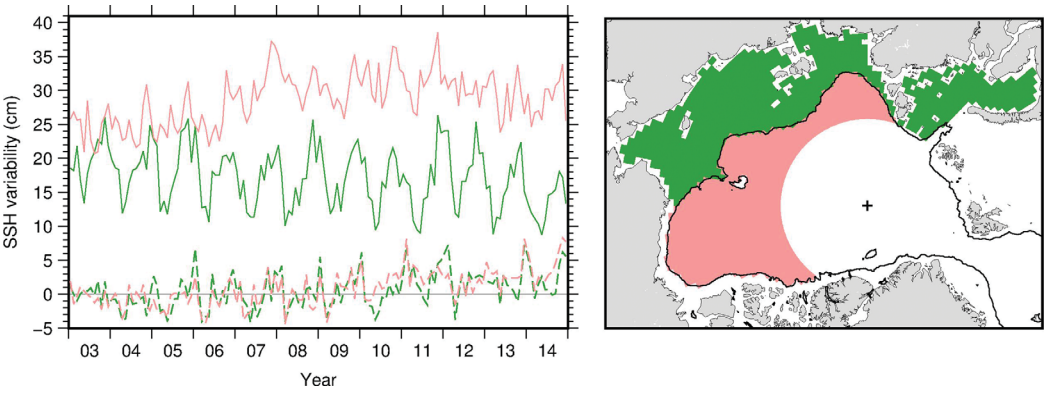

Figure 7. Steric height (solid line) and ocean mass (dashed line) for the Siberian shelf seas (Green) and the deep basin (pink), delineated by the 500 m isobath (black line on the map).

well as this, estimates of DOT in February/March 2004–2008 from the ICESat mission showed variable coverage on the Siberian shelf seas, due to a sparsity of lead tie points [*Kwok and Morison*, 2011]. The lack of year-round data in this region limits the conclusions that could be drawn about this important region of the Arctic Ocean. The monthly record of data from satellite altimetry and GRACE allows us to examine interannual and seasonal variability in steric height and ocean mass on the Siberian shelf seas for the first time. We calculate the monthly mean steric height and ocean mass over the Kara, Laptev, East Siberian, and Chukchi Seas, for depths less than 500 m. We exclude the Barents Sea from this analysis as sea level variability in this region has already been studied extensively [*Volkov et al.*, 2013]. Over the same sector of the Arctic Ocean (roughly 70°E–230°E), we also calculate the mean steric height and ocean mass for the deep basin (greater than 500 m depth) up to 81.5°N (Figure 7).

Ocean mass variations are coherent between the shelf seas and the deep basin, and show an overall increase between 2003 and 2014. However, the steric height on the Siberian shelf seas and the deep basin has diverged over the same time period. The increase in steric height in the deep basin is dominated by the large signal in the Beaufort Gyre, and shows a similar pattern of variability (increase between 2006 and 2008 and smaller decrease since 2011–2012; Figure 6). Steric height on the Siberian shelf seas shows large seasonal variation (amplitude 5.4 cm) and has steadily decreased over the course of the whole time series by 6.7 cm in the annual mean. Scaling by the area of study, this represents a decrease in FWC of $\sim$180 km^3. The detrended annual FWC anomaly of the Siberian shelves has a standard deviation of 30 km^3, which represents the interannual variability of FWC on the Siberian shelves during this period.

4.4. Arctic SSH Spatiotemporal Variability

We performed an Empirical Orthogonal Function (EOF) analysis to reveal the dominant modes of seasonal and nonseasonal Arctic SSH variability. EOFs are a commonly used tool for examining modes of statistically correlated spatiotemporal variability in gridded time series. We limit the analysis to the region shown in Figure 2 in order to limit the effects of SSH variation in the Nordic Seas and CAA that could be coupled to variability in the central Arctic (for analyses of SSH variability in the Nordic and Barents and Seas, see *Volkov et al.* [2013] and *Bulczak et al.* [2015]). We assess the significance of the separation of the EOF modes using the criteria of *North et al.* [1982]. EOF analysis was first performed on the full (seasonally varying) SSH data. The seasonal cycle contains the highest proportion of total variance, so we wish to inspect the spatial pattern associated with this variance. The leading two modes of seasonally varying SSH account for 62.6% of the total SSH variance and are both statistically separated. Next, the mean seasonal cycle was removed by subtracting the overall monthly mean SSH from each individual month at each grid point, and the EOF analysis repeated [*Peralta-Ferriz et al.*, 2014]. Figure 8 shows the leading seasonal and two leading nonseasonal modes of SSH variability, which are also statistically separated. We denote seasonal/nonseasonal EOFs and the associated principal component time series (PCs) with the subscripts *s*/*ns*, respectively, in the discussion below. EOF1$_s$ accounts for 38.7% of the total SSH variance, and together, the two leading modes of nonseasonal variability account for 55.4% of the remaining, nonseasonal, SSH variance. EOF2$_s$ and EOF1$_{ns}$ are essentially identical, representing 23.9/33.5% of the total/nonseasonal SSH variance. Here we refer to EOF1$_{ns}$, however PC2$_s$ is also

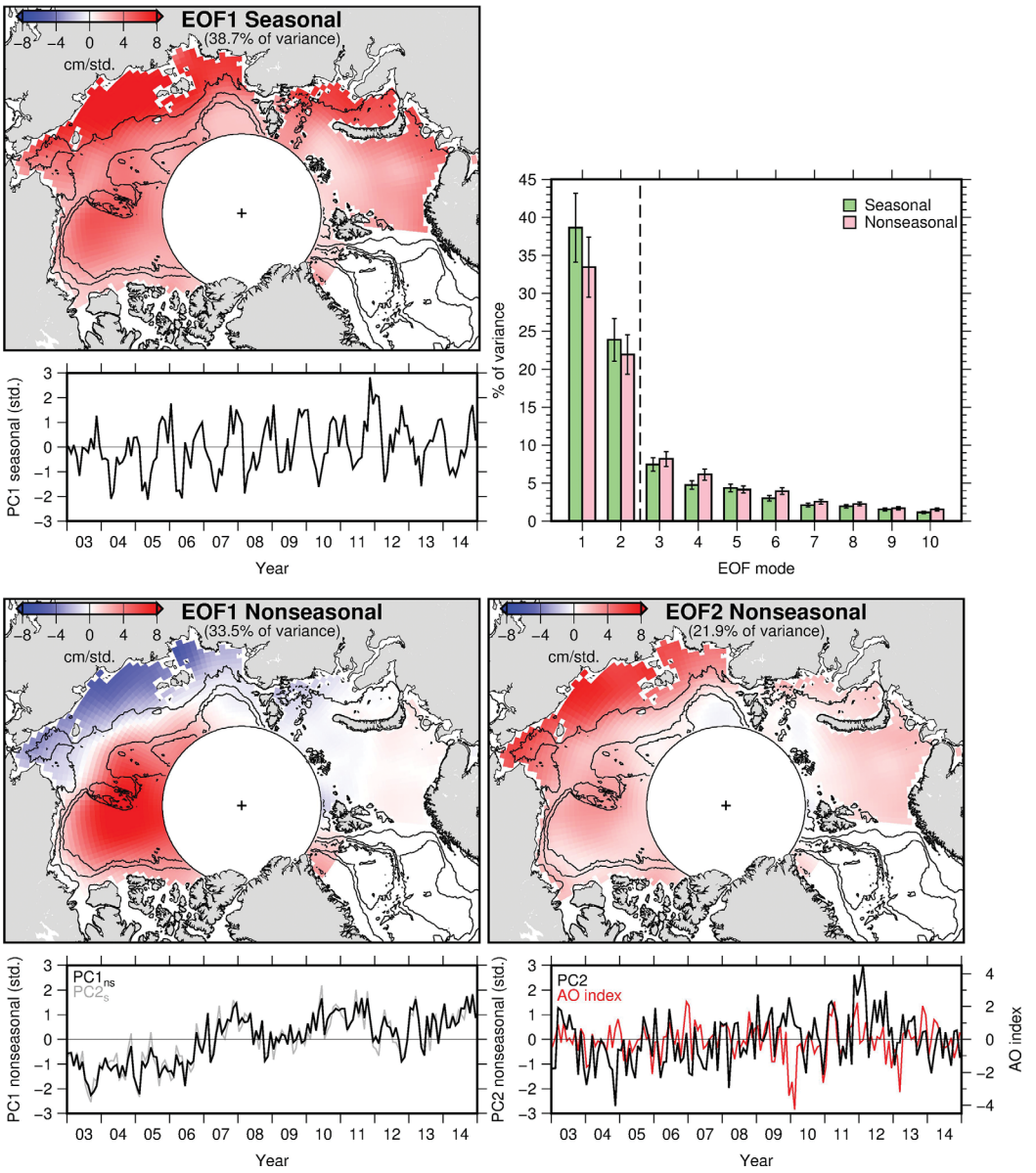

Figure 8. (top left) The first seasonal EOF mode and the (bottom left) first and (bottom right) second nonseasonal EOF modes of Arctic SSH and the corresponding PC time series'. Depth contours are drawn at 50, 1000, and 2500 m, taken from the ETOPO1 global bathymetry model [*Amante and Eakins*, 2009]. The first nonseasonal mode of SSH variability is essentially the same as the second seasonal mode of variability ($PC2_s$ is shown in grey (bottom left)). The AO index is superimposed on the second nonseasonal PC time series (red). The percentage of the SSH variance explained by the first 10 seasonal (green) and nonseasonal (pink) EOF modes is shown top right. The vertical dashed line indicates the threshold for significant modes proposed by *North et al.* [1982].

shown in Figure 8 for completeness; there is a small amount of additional, seasonal variance present in $PC2_s$ but it is small compared to the secular interannual variability that dominates this mode. $EOF2_{ns}$ is the final significant mode of SSH variability, accounting for 21.9% of nonseasonal SSH variance.

5. Discussion

5.1. Arctic SSH Seasonal Cycle

Arctic SSH variability is dominated by the seasonal cycle. The SSH time series analysis shows that the seasonal cycle is much larger than secular changes in this time period (Figure 5) and $EOF1_s$ captures 38.7% of the total SSH variance (Figure 8). $PC1_s$ is a maximum in early November and a minimum in May, on average, and takes a similar form to the altimeter time series (Figure 5). The RMS difference between the (total)

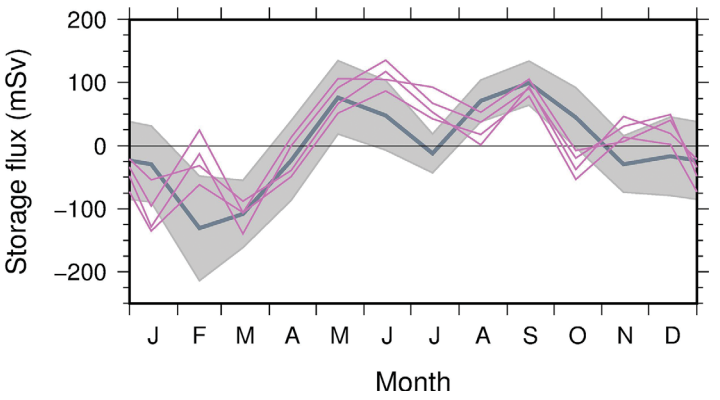

Figure 9. The satellite-derived (grey, shaded region is ±1 standard deviation) and modeled (magenta, reproduced with permission from *Bacon et al.* [2015]) Arctic Ocean storage flux seasonal cycle. Positive (negative) flux means a net flow into (out of) the blue shaded region in Figure 2 (100 mSv ≡ 10^5 m^3 s^{-1}).

mean SSH time series (Figure 5) and the SSH time series resulting from $EOF1_s$ alone is 0.8 cm. An analysis of the SSH seasonal range and phase shows a similar pattern to $EOF1_s$ (supporting information Figure S7)—large amplitude seasonal variations on the Siberian shelf seas and a basin-mean seasonal cycle that peaks in October–November on average.

It is instructive to examine the SSH seasonal cycle in terms of seasonal ocean storage fluxes. The SSH time series can be converted to a time series of ocean volume anomalies by multiplying by the surface area of the study region. The monthly mean SSH south of 81.5°N is representative of the basin mean SSH at monthly to seasonal time scales (supporting information Figures S2 and S3), so the area is taken to be that of the entire study region (9.81 × 10^{12} m^2, Figure 2). The additional uncertainty that results from only sampling south of 81.5°N is 0.69 cm (RMS), equivalent to an ocean volume uncertainty of 68 km^3, which is small compared to the 494 km^3 amplitude of the seasonal cycle. We then calculate the monthly ocean storage flux as the time derivative of the ocean volume anomaly time series, and estimate the mean seasonal cycle and standard deviation in the same way as for the seasonal cycles of SSH, ocean mass, and steric height (Figure 9). The ocean storage flux represents the sum of surface and boundary fluxes to the bounded Arctic Ocean domain (Figure 2) that result in seasonal changes in the volume of the Arctic Ocean. The magnitude (±100 mSv) and phase of the seasonal ocean storage flux calculated here agrees well with modeled results from *Bacon et al.* [2015], who took four model configurations with ∼3 and 9 km horizontal resolution, different atmospheric forcing and varying integration times and calculated seasonal cycles of the Arctic ocean storage fluxes (note that their study area included Baffin Bay, whereas it is excluded in the present study). Figure 9 compares the modeled results of *Bacon et al.* [2015] with SSH-derived results. The ocean storage flux from altimetry and its mean from the four model configurations are well correlated (R = 0.68). This generates confidence that both the model and the altimetry are performing well, and represents the first validation of model-derived ocean storage fluxes in the Arctic Ocean.

The largest component of the SSH seasonal cycle is the seasonal cycle of steric height. The seasonal cycle of ocean mass is smaller but causes an intermediate peak in SSH in June that is linked to the thawing of the terrestrial Arctic, which begins in May, and the large subsequent input of freshwater into the basin via river runoff [*Serreze et al.*, 2006]. The brief summertime increase in the ocean mass is not sustained: summertime freshwater flux from river runoff, precipitation minus evaporation (P-E), the relatively fresh Bering Strait inflow (which peaks in summer [*Woodgate et al.*, 2006]) and glacial meltwater from Greenland and the CAA forces denser seawater out through the boundaries of our ocean domain through the fast barotropic response to ocean mass input (we note, however, that the latter represents a small contribution to the Arctic Ocean freshwater budget, with an annual freshwater flux of ∼100 km^3 or less to the central Arctic [*Bamber et al.*, 2012]). Modeled results show that surface volume fluxes are nearly always in balance with ice and ocean boundary volume fluxes, and that the storage cycle is relatively small [*Bacon et al.*, 2015]. On the other hand, the typical residence time over which liquid freshwater circulates and exits the Arctic is around a decade on average [*Schlosser et al.*, 1994; *Ekwurzel et al.*, 2001]. The resulting overall freshening of the Arctic Ocean through summer by river runoff, P-E and sea ice melt is reflected in the steric height seasonal cycle, which rises through summer, peaking in October–November, and generally positive summertime ocean storage flux. The steric height then relaxes through winter as the surface ocean cools and sea ice is formed. The rejected brine makes the seawater denser, while the removal from the region of the lighter sea ice by

export through Fram Strait peaks in March [*Kwok et al.*, 2009]. Although sea ice begins to form in September in the central Arctic, steric height peaks in October–November as river runoff and P-E continue to be net freshwater inputs to the ocean until October [*Serreze et al.*, 2006]. The steric height seasonal cycle is larger than its interannual variability, whereas the ocean mass seasonal cycle is nearly always smaller than its interannual variability (Figure 5). Indeed, the interannual variability of the steric height seasonal cycle is smaller than our monthly steric height uncertainty estimate, suggesting that our uncertainty estimate is probably quite conservative. This complements the findings of *Volkov and Landerer* [2013] that nonseasonal SSH fluctuations at monthly time scales are due to ocean mass changes driven by atmospheric forcing; we find that steric height variations account for the largest part of the Arctic SSH seasonal cycle.

5.2. Secular Change

Between 2003 and 2011, steric height changes dominated annual mean SSH changes with our defined basin (Figure 5). There was a net accumulation of freshwater across the deep basins of the central Arctic [*Rabe et al.*, 2014], in particular, in the Beaufort Sea [*Proshutinsky et al.*, 2009; *Giles et al.*, 2012; *Krishfield et al.*, 2014] that we see reflected as a net increase in steric height. Between 2005 and 2008, there was a redistribution of freshwater from the Eurasian Basin to the Canada Basin [*Morison et al.*, 2012]. While Envisat captures the increasing freshwater content of the Canada Basin between 2005 and 2008, it does not capture the region north of 81.5° that saw some decrease (on the Eurasin Basin side) and some increase (on the Canada Basin side). We calculated the mean steric height by combining the ICESat DOT produced by *Kwok and Morison* [2011] and GRACE in the "pole hole;" however, there was not a significant change in mean steric height between 2004 and 2008. So, while our data do not capture patterns of spatial variability north of 81.5°N, the evidence from ICESat is that regional increases and decreases in steric height north of 81.5°N between 2004 and 2008 effectively cancel out. Between 2012 and 2014, the steric height dropped back to circa 2003 levels. To investigate whether this is caused by redistribution of freshwater back to the central Arctic basin (i.e., a reversal of the redistribution reported by *Morison et al.* [2012]), we examined the change in steric height from 2012 to 2014, utilizing the synoptic coverage provided by CryoSat-2 (Figure 10). The drop in steric height between 2012 and 2014 is dominated by large (>15 cm) reductions in the East Siberian and Laptev Seas, and small (close to zero) mean change inside the Envisat "pole hole." Between 2003 and 2014, the total secular change in SSH was determined by an overall increase in ocean mass of 2.1 ± 0.7 cm between 2003 and 2014.

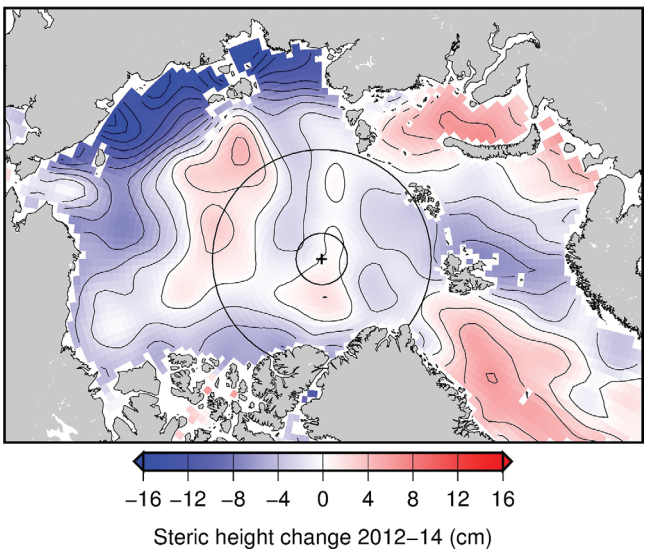

Figure 10. The change in annual mean steric height between 2012 and 2014 from CryoSat-2 and GRACE. The circles at 81.5°N and 88°N represent the latitudinal limit of Envisat and CryoSat-2, respectively. The data inside the CryoSat-2 "pole hole" is entirely interpolated.

5.3. Regional Freshwater Exchanges

The doming of SSH associated with a convergence of surface freshwater in the Beaufort Gyre clearly dominated the nonseasonal variability during this period, with $EOF1_{ns}$ representing 33.5% of the nonseasonal SSH variance. EOF analysis reveals that this doming was in fact concurrent with regional reductions in SSH in the Chukchi, East Siberian, Laptev, and eastern Kara Seas, mainly contained shoreward of the 50 m isobath. In section 4.3.3, this long-term divergence in SSH between the Siberian shelf seas and the deep basin was shown to be a steric signal. During this period, deepening of isopycnals and freshening of the Beaufort Gyre raised isopycnals in surrounding shelf seas, drawing more saline deep water further up the shelves. This is consistent with Ekman dynamics in the absence of a

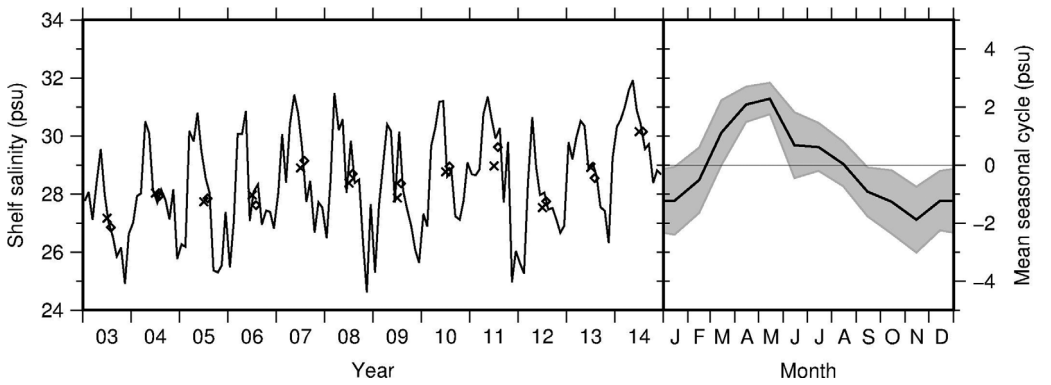

Figure 11. (left) The monthly mean (black line), annual mean (crosses), and summertime mean (June–September, diamonds) salinity of the Siberian shelf seas calculated from equation (6). (right) The mean seasonal cycle (black line). The shaded area represents ±1 standard deviation.

significant increase in regional freshwater sources; convergence of surface freshwater into one region is at least partially balanced by divergence from other regions. We see this reflected as an increase in ocean mass and a bulk densification of the water on the shelf seas.

It is possible to estimate a salinity anomaly time series for the shelf seas using the time series of steric height, and assuming that changes in steric height are dominated by salinity variations. The salinity anomaly, dS, can be written as:

$$dS = -\frac{1}{\beta D} d\eta_{steric} \tag{6}$$

where $\beta = (1/\rho)(d\rho/dS)$ is the haline expansion coefficient, D is the depth, and $d\eta_{steric}$ is the shelf seas steric height time series. We calculate the mean depth for each 2° × 0.5° longitude-latitude grid cell from the ETOPO1 global bathymetry model [*Amante and Eakins*, 2009] and use values of $d\rho/dS \sim 0.8$ kg m^{-3} psu^{-1} [*Gill*, 1982, Appendix 3] and $\rho \sim 1028$ kg m^{-3} [*Dmitrenko et al*., 2008]. We then take the area average over the Siberian shelf domain (Figure 7) and assume that the salinity anomaly is relative to the mean salinity of the deep ocean, i.e., $dS = S - S_{ref}$ (Figure 11). Here as is conventional, we choose $S_{ref} = 34.8$, however, this is essentially an arbitrary choice. As pointed out by *Bacon et al*. [2015], the only physically meaningful value of S_{ref} for the enclosed Arctic basin is the boundary mean salinity, which *Tsubouchi et al*. [2012] estimated to be 34.67. However, the choice of S_{ref} just contributes a static offset to the salinity time series shown in Figure 11, which is not relevant to the present study. We estimate the mean seasonal cycle and its interannual variability as earlier and also calculate the annual and hydrographic summertime means (June–September). The detrended annual mean shelf salinity has a standard deviation of 0.6 psu, a response to interannual variability of runoff, sea ice volume and P-E. The standard deviation of the difference between the summertime and annual means is 0.3 psu. Indeed, *Dmitrenko et al*. [2008] remarked that interannual variability in salinity anomalies derived from ship-based measurements are dominated by space and time sampling errors. This is compounded by the fact that the salinity reduces significantly between May and November (by ∼4 psu on average) due to summertime freshwater inputs; hydrographic measurements made during summer will be highly sensitive to the timing of the seasonal onset of sea ice melt and river input.

Dmitrenko et al. [2008] found that salinity and FWC anomalies on the Siberian shelf seas are modulated by the prevailing atmospheric circulation, observing positive/negative salinity anomalies (negative/positive FWC anomalies) during periods of predominantly anticyclonic/cyclonic atmospheric circulation. This is apparent in our data: during the entire time series, the Anticyclonic Circulation Regime dominated Arctic circulation [*Proshutinsky et al*., 2015] and the mean salinity of the Siberian shelf seas, which we here extend to include the Chukchi and Kara Seas, increased by 0.15 psu yr^{-1}. *Dmitrenko et al*. [2008] estimated that between periods of anticyclonic and cyclonic atmospheric circulation, the East Siberian and Laptev Seas exchange about 500 km^3 of freshwater with the deep basin. However, our estimate of the total FWC loss from the shelf seas between 2003 and 2014 (∼180 km^3) is rather small. While the shelf seas receive large freshwater inputs from rivers, their buffering capacity is small, even given their residence time of a few years [*Schlosser et al*., 1994]. Thus, the contribution of freshwater redistribution within the Arctic basin is small

compared to the total freshwater accumulation in the Beaufort Gyre region; at least one order of magnitude smaller for exchanges with the shelf seas, with no net change in steric height observed within the "pole hole" (section 5.2 and Figure 10). Most of the freshwater accumulation in the Beaufort Gyre, therefore, is a consequence of reduction of freshwater export from the Arctic Ocean. This observation is in agreement with the study of *Koldunov et al*. [2014], who found that Beaufort Gyre freshwater accumulation is dominated by Ekman convergence and a reduction of freshwater outflow through the CAA, rather than through redistribution of shelf water to the Canada Basin. They found that simulated upper-50 m horizontal freshwater flux through the CAA was reduced or even reversed in 2005–2009 relative to 1970–2000 due to increased Ekman convergence in the Beaufort Sea. Using typical figures for the Beaufort Gyre freshwater accumulation, a ~5000 km^3 increase in FWC over ~5 years represents a net reduction in freshwater export of about 30 mSv, or 15% for an Arctic Ocean mean boundary flux of 200 mSv [*Bacon et al*., 2015].

5.4. Nonseasonal Ocean Mass Variability on the Siberian Shelf Seas

$EOF2_{ns}$ is dominated by a center of action on the Chukchi, East Siberian and Laptev shelf seas, predominantly shoreward of the 50 m isobath, which accounts for 21.9% of nonseasonal SSH variance. This spatial pattern of variability is very similar to the second EOF of GRACE data found by *Peralta-Ferriz et al*. [2014] and the first coupled EOF of ocean mass and zonal wind stress found by *Volkov and Landerer* [2013], with the notable difference that here we do not observe a concurrent drop in SSH in the central Arctic due to the latitudinal limit of the altimetry data. It is also a very similar spatial pattern of variability to $EOF1_s$, with more weight on the shelf seas and less weight elsewhere in the Arctic. This implies that $EOF2_{ns}$ captures the nonseasonal ocean mass fluctuations superimposed on the more steady seasonal cycle of steric height evident in $EOF1_s$.

When $PC2_{ns}$ is regressed onto monthly sea level pressure (SLP), we find the same pattern of correlation as in *Peralta-Ferriz et al*. [2014]: low SLP anomalies over the central Arctic and high SLP anomalies over northern Europe and Russia. This drives westerly wind anomalies along the coast of northern Russia that cause onshore Ekman pumping and an accumulation of water on the Siberian shelves [*Volkov and Landerer*, 2013; *Peralta-Ferriz et al*., 2014]. *Peralta-Ferriz et al*. [2014] found that this mode of variability was significantly correlated to the Arctic Oscillation (AO) index. A positive AO index indicates low atmospheric pressure over the central Arctic, which is responsible for driving the eastward alongshore wind anomalies in the Siberian Arctic [*Peralta-Ferriz et al*., 2014]. We find a weak, but significantly nonzero, correlation ($R = 0.18$, $p = 0.03$) between $PC2_{ns}$ and the AO index (Figure 8); the reduced correlation is likely because of the steric signal present in the altimeter data. $PC1_{ns}$ and $PC2_{ns}$ both increase between 2004 and 2012; however, the direction of change is in opposite directions on the Siberian shelf seas—decreasing in $EOF1_{ns}$ and increasing in $EOF2_{ns}$. This reflects the opposing trends in ocean mass (increasing) and steric height (decreasing) on the Siberian shelves (Figure 7) and the fact that $EOF1_{ns}$ captures largely steric variability and $EOF2_{ns}$ captures ocean mass variability. The reduction of $PC2_{ns}$ after 2012 is probably due to contamination of the ocean mass signal with the large reduction in steric height between 2012 and 2014 (Figure 10).

6. Conclusions

We have presented the first basin-wide estimates of monthly SSH in the Arctic Ocean from satellite altimetry utilizing data from both the ice-free and ice-covered ocean. Steric heights between 2003 and 2014 have been estimated by combining SSH with ocean mass data. SSH estimates from altimetry show good overall agreement with tide gauge data in regions of seasonal ice cover ($R = 0.65$) and excellent agreement in areas that are permanently ice free ($R = 0.89$), satellite-derived steric height estimates agree well with GPH estimated from ITPs and the 2003 and 2014 mean Arctic DOT shows qualitative agreement with previous observational and modeling studies. The seasonal cycle of Arctic SSH accounts for 38.7% of the total SSH variance; it is larger than secular changes during this time period and is dominated by a regular seasonal cycle of steric height associated with seasonal fluxes of freshwater. An amplitude of ~5 cm agrees well with simple considerations of seasonal surface and boundary fluxes [*Aagaard and Carmack*, 1989; *Bacon et al*., 2015]. Between 2003 and 2012, the steric height increased due to a freshening of the Arctic Ocean during the 2000s [*Proshutinsky et al*., 2009; *Giles et al*., 2012; *Krishfield et al*., 2014; *Rabe et al*., 2014]. The steric height peaked in 2012 and subsequently dropped to 2003 levels by the end of our time series, representing a total increase, and decrease, of 2.2 ± 1.4 cm. The drop in steric height between 2012 and 2014 was dominated by large (>15 cm) reductions in the East Siberian and Laptev Seas. By the end of the time series the total secular increase in SSH is due to an increase in ocean mass of 2.1 ± 0.7 cm between 2003 and 2014.

Doming of SSH in the Beaufort Gyre dominated nonseasonal SSH variability in this time period, accounting for 33.5% of the nonseasonal SSH variance. We find that SSH in the Beaufort Gyre has stayed at a roughly constant level since the dramatic increase in the 2000s reported by *Giles et al*. [2012]. However, since ~2011–2012, regional ocean mass increases mean that the steric height has dropped since 2012. We estimate that the steric height peaked in 2010, representing a freshwater accumulation of 4600 km^3 relative to the 2003–2006 mean. By 2014, the Beaufort Gyre FWC was just 1700 km^3 greater than the 2003–2006 mean, as a result of the weaker Anticyclonic Circulation Regime since 2011 [*Proshutinsky et al*., 2015]. The Beaufort Gyre region has a seasonal FWC cycle of ±2000 km^3 (equivalent to a freshwater layer of ±1.1 m) which agrees well with hydrographic observations from moored profilers [*Proshutinsky et al*., 2009]. Doming of SSH in the Beaufort Gyre is concurrent with regional drops in SSH in the East Siberian, Laptev and eastern Kara Seas, demonstrating that lowering of isopycnals associated with freshening of the Canada Basin is partially compensated for by raising of isopycnals in the peripheral seas, in agreement with [*Morison et al*., 2012]. There was a net reduction of ~180 km^3 of freshwater from the Siberian shelf seas during our study period and an increase in depth integrated salinity of 0.15 psu yr^{-1}. Small net changes in steric height within the Envisat "pole hole" from the ICESat mission and from CryoSat-2 between 2012 and 2014 indicate that overall, freshwater redistribution within the Arctic basins contributed little to the overall accumulation during the 2000s. Rather, this was caused by a dynamic reduction of freshwater export from the Arctic of order 15% (30 mSv).

The Siberian shelf seas have a large steric height seasonal cycle that reflects seasonal salinity variability due to river runoff (±2psu on average). Nonseasonal SSH variability in this region accounts for 21.9% of the nonseasonal SSH variance and is caused by zonal wind anomalies along the Siberian coastline that drive onshore Ekman transport and ocean mass anomalies on the Siberian shelf seas. This mode of variability resembles a leading mode of GRACE ocean mass variability [*Volkov and Landerer*, 2013; *Peralta-Ferriz et al*., 2014] and resembles the spatial amplitude of the SSH seasonal cycle. Thus, we interpret this mode of variability as nonseasonal ocean mass fluctuations that are superimposed on the more regular seasonal cycle of steric height, complimenting the finding of *Volkov and Landerer* [2013] that monthly SSH fluctuations are wind-forced ocean mass changes.

Finally, we have demonstrated that monthly altimeter SSH can be used to estimate the Arctic Ocean storage flux: the rate at which the Arctic Ocean volume increases (during summer) and decreases (during winter). The seasonal phase, and amplitude of 100 mSv, agrees well with high-resolution modeled results [*Bacon et al*., 2015]. Since monthly ocean storage fluxes are closely related to the Arctic freshwater cycle, monthly SSH from altimetry offers a valuable tool for future monitoring of the Arctic hydrological cycle, particularly if combined with either models or other measurement techniques.

Acknowledgments

The authors would like to acknowledge the contributions of Seymour Laxon and Katharine Giles, without whom the present work would not be possible. This work was supported by a U.K. Natural Environment Research Council (NERC) studentship and this manuscript is a contribution to the NERC Arctic Research Programme TEA-COSI project (http://teacosi.org/). Radar altimetry data were supplied by the European Space Agency (https://earth.esa.int/web/guest/data-access/) and GRACE data were supplied by the Jet Propulsion Laboratory (http://grace.jpl.nasa.gov/data/). ICESat DOT is available via the Jet Propulsion Laboratory (http://rkwok.jpl.nasa.gov/icesat/data_topography.html). Tide gauge data are from the Permanent Service for Mean Sea Level (http://www.psmsl.org/). The Ice-Tethered Profiler data were collected and made available by the Ice-Tethered Profiler Program [*Toole et al*., 2011; *Krishfield et al*., 2008] based at the Woods Hole Oceanographic Institution (http://www.whoi.edu/itp). The GOCO03s geoid model was provided by the Gravity Observation Combination project (http://www.goco.eu/). DOT data presented in this manuscript can be accessed via http://www.cpom.ucl.ac.uk/dynamic_topography.

References

Aagaard, K., and E. Carmack (1989), The role of sea ice and other fresh water in the Arctic circulation, *J. Geophys. Res.*, *94*, 14,485–14,498, doi:10.1029/JC094iC10p14485.

Amante, C., and B. W. Eakins (2009), ETOPO1 1 arc-minute global relief model: Procedures, data sources and analysis, *NOAA Tech. Memo. NESDIS NGCD-24*, Natl. Geophys. Data Cent., NOAA, doi:10.7289/V5C8276M. [Available at: http://www.ngdc.noaa.gov/docucomp/page?xml=NOAA/NESDIS/NGDC/MGG/DEM/iso/xml/316.xml&view=getDataView&header=none.]

Bacon, S., Y. Askenov, S. Fawcett, and G. Madec (2015), Arctic mass, freshwater and heat fluxes: Methods, and modelled seasonal variability, *Philos. Trans. R. Soc. A*, *373*, doi:10.1098/rsta.2014.0169.

Bamber, J., M. van Den Broeke, J. Ettema, J. Lenaerts, and E. Rignot (2012), Recent large increases in freshwater fluxes from Greenland into the North Atlantic, *Geophys. Res. Lett.*, *39*, L19501, doi:10.1029/2012GL052552.

Belkin, I. (2004), Propagation of the ''Great Salinity Anomaly'' of the 1990s around the northern North Atlantic, *Geophys. Res. Lett.*, *31*, L08306, doi:10.1029/2003GL019334.

Belkin, I. M., S. Levitus, J. Antonov, and S.-A. Malmberg (1998), "Ggreat Salinity Anomalies" in the North Atlantic, *Prog. Oceanogr.*, *41*, 1–68, doi:10.1016/S0079-6611(98)00015-9.

Bulczak, A. I., S. Bacon, A. C. Naveira Garabato, A. Ridout, M. J. P. Sonnewald, and S. W. Laxon (2015), Seasonal variability of sea surface height in the coastal waters and deep basins of the Nordic Seas, *Geophys. Res. Lett.*, *42*, 113–120, doi:10.1002/2014GL061796.

Chambers, D. P., and J. A. Bonin (2012), Evaluation of Release-05 GRACE time-variable gravity coefficients over the ocean, *Ocean Sci.*, *8*, 859–868, doi:10.5194/os-8-859-2012.

Dee, D. P., et al. (2011), The ERA-Interim reanalysis: Configuration and performance of the data assimilation system, *Q. J. R. Meteorol. Soc.*, *137*, 553–597, doi:10.1002/qj.828.

Dickson, R. R., J. Meincke, S.-A. Malmberg, and A. J. Lee (1988), The "Great Salinity Anomaly" in the northern North Atlantic 1968–1982, *Prog. Oceanogr.*, *20*, 103–151, doi:10.1016/0079-6611(88)90049-3.

Dmitrenko, I. A., S. A. Kirillov, and L. B. Tremblay (2008), The long-term and interannual variability of summer fresh water stroage over the eastern Siberian shelf: Implications for climate change, *J. Geophys. Res.*, *113*, C03007, doi:10.1029/2007JC004304.

Drinkwater, M. R. (1991), K*u* band airborne radar altimeter observations of marginal sea ice during the 1984 marginal ice zone experiment, *J. Geophys. Res.*, *96*, 4555–4572, doi:10.1029/90JC01954.
Ekwurzel, B., P. Schlosser, R. A. Mortlock, and R. G. Fairbanks (2001), River runoff, sea ice meltwater, and Pacific water distribution and mean residence times in the Arctic Ocean, *J. Geophys. Res.*, *106*, 9075–9092, doi:10.1029/1999JC000024.
European Space Agency (2015), Geophysical corrections in level 2 CryoSat data products, IDEAS-VEG-IPF-MEM-1288 Version 5.0, ESRIN, Italy.
Farrell, S. L., D. C. McAdoo, S. W. Laxon, H. J. Zwally, D. Li, A. Ridout, and K. Giles (2012), Mean dynamic topography of the arctic ocean, *Geophys. Res. Lett.*, *39*, L01601, doi:10.1029/2011GL050052.
Giles, K. A., S. W. Laxon, D. J. Wingham, D. W. Wallis, W. B. Krabill, C. J. Leuschen, D. McAdoo, S. S. Manizade, and R. K. Raney (2007), Combined airborne laser and radar altimeter measurements over the Fram Strait in May 2002, *Remote Sens. Environ.*, *111*, 182–194.
Giles, K. A., S. W. Laxon, and A. L. Ridout (2008), Circumpolar thinning of the Arctic sea ice following the 2007 record ice extent minimum, *Geophys. Res. Lett.*, *35*, L22502, doi:10.1029/2008GL035710.
Giles, K. A., S. W. Laxon, A. L. Ridout, D. J. Wingham, and S. Bacon (2012), Western Arctic Ocean freshwater storage increased by wind-driven spin-up of the Beaufort Gyre, *Nat. Geosci.*, *5*, 194–197, doi:10.1038/ngeo1379.
Gill, A. E. (1982), *Atmosphere–Ocean Dynamics*, Academic, San Diego, Calif.
Häkkinen, S. (1993), An Arctic sources for the Great Salinity Anomaly: A simulation of the Arctic ice-ocean system for 1955-1975, *J. Geophys. Res.*, *98*, 16,397–16,410, doi:10.1029/93JC01504.
Holgate, S. J., A. Matthews, P. L. Woolworth, L. J. Rickards, M. E. Tamisiea, E. Bradshaw, P. R. Foden, K. M. Gordon, S. Jevrejeva, and J. Pugh (2013), New data systems and products at the Permanent Service for Mean Sea Level, *J. Coastal Res.*, *29*, 493–504, doi:10.2112/JCOASTRES-D-12-00175.1.
IPCC (2013), *Climate Change 2013: The Physical Science Basis*, 1535 pp., Cambridge Univ. Press, N. Y.
Koldunov, N. V., et al. (2014), Multimodel simulations of Arctic Ocean sea surface height variability in the period 1970-2009, *J. Geophys. Res. Oceans*, *119*, 8936–8954, doi:10.1002/2014JC010170.
Krishfield, R., J. Toole, A. Proshutinsky, and M.-L. Timmermans (2008), Automated Ice-Tethered Profilers for seawater observations under pack ice in all seasons, *J. Atmos. Ocean. Technol.*, *25*, 2091–2105, doi:10.1175/2008JTECHO587.1.
Krishfield, R. A., A. Proshutinsky, K. Tateyama, W. J. Williams, E. C. Carmack, F. A. McLaughlin, and M.-L. Timmermans (2014), Deterioration of perennial sea ice in the Beaufort Gyre from 2003 to 2012 and its impact on the oceanic freshwater cycle, *J. Geophys. Res. Oceans*, *119*, 1271–1305, doi:10.1002/2013JC008999.
Kurtz, N. T., N. Galin, and M. Studinger (2014), An improved CryoSat-2 sea ice freeboard retrieval algorithm through the use of waveform fitting, *Cryosphere*, *8*, 1217–1237, doi:10.5194/tc-8-1217-2014.
Kwok, R., and J. Morison (2011), Dynamic topography of the ice–covered Arctic Ocean from ICESat, *J. Geophys. Res.*, *38*, L02501, doi:10.1029/2010GL046063.
Kwok, R., and J. Morison (2015), Sea surface height and dynamic topography of the ice-covered oceans from CryoSat-2: 2011–2014, *J. Geophys. Res. Oceans*, *121*, 674–692, doi:10.1002/2015JC011357.
Kwok, R., G. F. Cunningham, M. Wensnahan, I. Rigor, H. J. Zwally, and D. Yi (2009), Thinning and volume loss of the Arctic Ocean sea ice cover: 2003–2008, *J. Geophys. Res.*, *114*, C07005, doi:10.1029/2009JC005312.
Laxon, S. (1994), Sea ice altimeter processing scheme at the EODC, *Int. J. Remote Sens.*, *15*, 915–924, doi:10.1080/01431169408954124.
Laxon, S., and D. McAdoo (1994), Arctic Ocean gravity field derived from ERS-1 satellite altimetry, *Science*, *265*(5172), 621–624, doi:10.1126/science.265.5172.621.
Laxon, S. W., et al. (2013), CryoSat-2 estimates of Arctic sea ice thickness and volume, *Geophys. Res. Lett.*, *40*, 732–737, doi:10.1002/grl.50193.
Manabe, S., and R. J. Stouffer (1995), Simulation of abrupt climate change induced by freshwater input to the North Atlantic, *Nature*, *378*, 165–167, doi:10.1038/378165a0.
Martin, T., M. Steele, and J. Zhang (2014), Seasonality and long-term trend of Arctic Ocean surface stress in a model, *J. Geophys. Res. Oceans*, *119*, 1723–1738, doi:10.1002/2013JC009425.
Mayer-Gürr, T., et al. (2012), The new combined satellite only model GOCO03s, poster presented at GGHS2012 meeting, Gravity Observation and Combination project, initiated by the ESA GOCE AO (project no. 4248), Venice, Italy.
Mizobata, K., E. Watanabe, and N. Kimura (2016), Wintertime variability of the Beaufort gyre in the Arctic Ocean derived from CryoSat-2/SIRAL observations, *J. Geophys. Res. Oceans*, *121*, 1685–1699, doi:10.1002/2015JC011218.
Morison, J., M. Steele, T. Kikuchi, K. Falkner, and W. Smethie (2006), Relaxation of central Arctic Ocean hydrography to pre-1990s climatology, *Geophys. Res. Lett.*, *33*, L17604, doi:10.1029/2006GL026826.
Morison, J., J. Wahr, R. Kwok, and C. Peralta-Ferriz (2007), Recent trends in Arctic Ocean mass distribution revealed by GRACE, *Geophys. Res. Lett.*, *34*, L07602, doi:10.1029/2006GL029016.
Morison, J., R. Kwok, C. Peralta-Ferriz, M. Alkire, I. Rigor, R. Andersen, and M. Steele (2012), Changing Arctic Ocean freshwater pathways, *Nature*, *481*, 66–70, doi:10.1038/nature10705.
North, G. R., T. L. Bell, and R. F. Cahalan (1982), Sampling errors in the estimation of empirical orthogonal functions, *Mon. Weather Rev.*, *110*, 699–706, doi:10.1175/1520-0493(1982)110 < 0699:SEITEO > 2.0.CO;2.
Ollivier, A., Y. Faugere, N. Picot, M. Ablain, P. Femenias, and J. Benveniste (2012), Envisat ocean altimeter becoming relevant for mean sea level trend studies, *Mar. Geod.*, *35*, 118–136, doi:10.1080/01490419.2012.721632.
Peacock, N. R., and S. W. Laxon (2004), Sea surface height determination in the Arctic Ocean from ERS altimetry, *J. Geophys. Res.*, *109*, C07001, doi:10.1029/2001JC001026.
Peralta-Ferriz, C., and J. Morison (2010), Understanding the annual cycle of the Arctic Ocean bottom pressure, *Geophys. Res. Lett.*, *37*, L10603, doi:10.1029/2010GL042827.
Peralta-Ferriz, C., J. H. Morison, J. M. Wallace, J. A. Bonin, and J. Zhang (2014), Arctic Ocean circulation patterns revealed by GRACE, *J. Clim.*, *27*, 1445–1468, doi:10.1175/JCLI-D-13-00013.1.
Prandi, P., M. Ablain, A. Cazenave, and N. Picot (2012), A new estimation of mean sea level in the Arctic Ocean from satellite altimetry, *Mar. Geod.*, *35*, 61–81, doi:10.1080/01490419.2012.718222.
Proshutinsky, A., I. M. Ashik, E. N. Dvorkin, S. Häkkinen, R. A. Krishfield, and W. R. Peltier (2004), Secular sea level change in the Russian sector of the Arctic Ocean, *J. Geophys. Res.*, *109*, C03042, doi:10.1029/2003JC002007.
Proshutinsky, A., R. Krishfield, M.-L. Timmermans, J. Toole, E. Carmack, F. McLaughlin, W. J. Williams, S. Zimmerman, M. Itoh, and K. Shimada (2009), Beaufort Gyre freshwater reservoir: State and variability from observations, *J. Geophys. Res.*, *114*, C00A10, doi:10.1029/2008JC005104.

Proshutinsky, A., D. Dukhovsky, M. Timmermans, R. Krishfield, and J. L. Bamber (2015), Arctic circulation regimes, *Philos. Trans. R. Soc. A*, *373*, doi:10.1098/rsta.2014.0160.

Rabe, B., M. Karcher, F. Kauker, U. Schauer, J. M. Toole, R. A. Krishfield, T. Pisarev, S. Kikuchi, and J. Su (2014), Arctic Ocean basin liquid freshwater storage trend 1992–2012, *Geophys. Res. Lett.*, *41*, 961–968, doi:10.1002/2013GL058121.

Richter, K., J. E. Ø. Nilsen, and H. Drange (2012), Contributions to sea level variability along the Norwegian coast for 1960–2010, *J. Geophys. Res.*, *117*, C05038, doi:10.1029/2011JC007826.

Ridout, A. (2014), New mean sea surface for the CryoSat-2 L2 SAR chain, *Technical Note C2-TN-UCL-BC-0003*, issue 1.0, CPOM, Univ. College London, London, U. K.

Schlosser, P., D. Bauch, R. Fairbanks, and G. Bönisch (1994), Arctic river runoff: Mean residence time on the shelves and in the halocline, *Deep Sea Res., Part I*, *41*, 1053–1068, doi:10.1016/0967-0637(94)90018-3.

Serreze, M. C., and R. G. Barry (2011), Processes and impacts of Arctic amplification: A research synthesis, *Global Planet. Change*, *77*, 85–96, doi:10.1016/j.gloplacha.2011.03.004.

Serreze, M. C., A. P. Barrett, A. G. Slater, R. A. Woodgate, K. Aagaard, R. B. Lammers, M. Steele, R. Moritz, M. Meredith, and C. M. Lee (2006), The large-scale freshwater cycle of the Arctic, *J. Geophys. Res.*, *111*, C11010, doi:10.1029/2005JC003424.

Serreze, M. C., A. P. Barrett, J. C. Stroeve, D. N. Kindig, and M. M. Holland (2009), The emergence of surface-based Arctic amplification, *Cryosphere*, *3*, 11–19, doi:10.5194/tc-3-11-2009.

Soussi, B., S. Urien, F. Soulat, A. Muir, M. Roca, and D. Cotton (2011), *ENVISAT ALTIMETRY Level 2 User Manual*, version 1.4, edited by P. Féménias, Eur. Space Agency. [Available at: envisat.esa.int/handbooks/.]

Stroeve, J. C., V. Kattsov, A. Barrett, M. Serreze, T. Pavlova, M. Holland, and W. N. Meier (2012), Trends in Arctic sea ice extent from CMIP5, CMIP3 and observations, *Geophys. Res. Lett.*, *39*, L16502, doi:10.1029/2012GL052676.

Toole, J. M., R. A. Krishfield, M. Timmermans, and A. Proshutinsky (2011), The Ice-Tethered Profiler: Argo of the Arctic, *Oceanaography*, *24*, 126–135, doi:10.5670/oceanog.2011.64.

Tsubouchi, T., S. Bacon, A. C. Naveira Garabato, Y. Aksenov, S. W. Laxon, E. Fahrbach, A. Beszczynska-Möller, E. Hansen, C. M. Lee, and R. B. Ingvaldsen (2012), The Arctic Ocean in summer: A quasi-synoptic inverse estimate of boundary fluxes and water mass transformation, *J. Geophys. Res.*, *117*, C01024, doi:10.1029/2011JC007174.

Volkov, D., and F. W. Landerer (2013), Nonseasonal fluctuations of the Arctic Ocean mass observed by the GRACE satellites, *J. Geophys. Res.*, *118*, 6451–6460, doi:10.1002/2013JC009341.

Volkov, D. L., F. W. Landerer, and S. A. Kirillov (2013), The genesis of sea level variability in the Barents Sea, *Cont. Shelf Res.*, *66*, 92–104, doi:10.1016/j.csr.2013.07.007.

Wingham, D. J., et al. (2006), CryoSat: A mission to determine the fluctuations in the Earth's land and marine ice fields, *Adv. Space Res.*, *37*, 841–871.

Woodgate, R. A., K. Aagaard, and T. J. Weingartner (2006), Interannual changes in the Bering Strait fluxes of volume, hear and freshwater between 1991 and 2004, *Geophys. Res. Lett.*, *33*, L15609, doi:10.1029/2006GL026931.